Research Square

Preprints are preliminary reports that have not undergone peer review.
They should not be considered conclusive, used to inform clinical practice,
or referenced by the media as validated information.

Microstructure Evolution and Synergistic Optimization of Mechanical Properties and Thermal Conductivity in Mg-xSn-0.2Ca-0.5Zr Alloys

Chunyu Wang
Aviation Maintenance NCO Academy, Air Force Engineering University
Hefu Tan
Shenyang University of Technology
Hongbao Li
Shenyang University of Technology
Xudong Du
dxd9297@126.com
Shenyang University of Technology
Feng Wang
Shenyang University of Technology

Research Article

Keywords: Mg-Sn-Ca alloy, Semi-solid rheo-die casting, Mechanical Properties, Thermal conductivity, Microstructure

Posted Date: October 26th, 2026

DOI: https://doi.org/10.21203/rs.3.rs-11315565/v1

License: This work is licensed under a Creative Commons Attribution 4.0 International License.
Read Full License

Additional Declarations: No competing interests reported.

Microstructure Evolution and Synergistic Optimization of Mechanical Properties and Thermal Conductivity in Mg-xSn-0.2Ca-0.5Zr Alloys

Chunyu Wang[1], Hefu Tan[2, 3, 4], Hongbao Li [2, 3, 4], Xudong Du [2, 3, 4, *], Feng Wang[2, 3, 4]

1 Aviation Maintenance NCO Academy, Air Force Engineering University, Xinyang 464001, China
2 School of Materials Science and Engineering, Shenyang University of Technology, Shenyang 110870, China
3 Key Laboratory of Magnesium Alloys and the Processing Technology of Liaoning Province, Shenyang 110870, China
4 Automobile Lightweight Technology Professional Innovation Center of Liaoning Province, Tieling 112600, China
*Correspondence: dxd9297@126.com

Abstract:

To address the challenge of the trade-off between mechanical properties and thermal conductivity in magnesium alloys, Mg-xSn-0.2Ca-0.5Zr alloys (x = 3, 4, 5 wt.%) were investigated in this work. Permanent mold casting, semi-solid rheo-die casting, and heat treatment were employed to tailor the microstructure of the alloys. The inherent correlations between microstructure evolution, mechanical properties, and thermal conductivity were systematically explored. The results reveal that as Sn content increases in permanent mold cast alloys, grain refinement occurs and the volume fraction of secondary phases rises. Nevertheless, excessive Sn induces coarsening of grain-boundary Mg_2Sn, thereby degrading both ductility and thermal conductivity. Among the permanent mold cast alloys, Mg-4Sn-0.2Ca-0.5Zr exhibits optimal overall performance, with an ultimate tensile strength of 137 MPa, yield strength of 71 MPa, elongation of 7.6%, and thermal conductivity of 86.12 W/(m·K), and is accompanied by the lowest hot-tearing susceptibility. Near-spherical α-Mg grains are obtained in the semi-solid rheo-die cast Mg-4Sn-0.2Ca-0.5Zr alloy. After T6 heat treatment, fine Mg_2Sn precipitates are dispersed throughout the matrix. The ultimate tensile strength, yield strength, and elongation are improved to 202 MPa, 112 MPa, and 11.7%, respectively. Meanwhile, aging facilitates the precipitation of Sn from the α-Mg matrix

and reduces electron scattering, contributing to an elevated thermal conductivity of 110.68 W/(m·K). Regulation of the solidification microstructure enables the simultaneous enhancement of strength, ductility, and thermal conductivity for Mg-Sn-Ca-Zr alloys.

Keywords: Mg-Sn-Ca alloy, Semi-solid rheo-die casting, Mechanical Properties, Thermal conductivity, Microstructure

1. Introduction

With the development of aerospace, new energy vehicles, and high-power electronic devices toward greater lightweighting and higher power density, lightweight metallic components are evolving from simple load-bearing functions to integrated structural-thermal management, which imposes higher requirements on the strength, ductility, and thermal conductivity of materials [1, 2]. Magnesium (Mg) alloys feature low density, high specific strength, and excellent damping capacity as well as relatively high specific thermal conductivity compared with other non-ferrous alloys, making them promising candidate materials for integrated lightweight structural and thermal management applications [3-6]. Among them, Mg-Sn-Ca-based alloys feature low cost, rare-earth-free composition, diverse phase constituents, and microstructure tunability via precipitation behavior. Therefore, they are regarded as one of the promising heat-treatable strengthened Mg alloy systems [7]. The solid solubility of Sn in Mg changes significantly with temperature; Mg_2Sn precipitates upon aging after solution treatment, while the addition of Ca facilitates the formation of thermally stable phases, including CaMgSn, and alters the composition and thermal stability of grain-boundary second phases [8-10]. The phase equilibria and solidification paths of the Mg-Sn-Ca ternary system have been relatively well described from a thermodynamic perspective [11]. Further studies [9] demonstrate that tuning the Sn/Ca ratio can alter the composition and distribution of phases, including Mg_2Sn, CaMgSn, and Mg_2Ca in the alloy, thereby significantly affecting its strength, ductility, and high-temperature stability. Nevertheless, the beneficial effect of Sn is not monotonically enhanced with its rising

content. Moderate Sn addition increases resistance to plastic deformation through grain refinement and a higher volume fraction of second phases, including Mg_2Sn. In contrast, excess Sn leads to abundant coarse second phases, increasing local stress concentrations and susceptibility to crack initiation, thereby impairing strength–ductility synergy. Meanwhile, variations in the matrix solute Sn content and the number of second-phase interfaces can alter the scattering behavior of electrons and phonons, thereby significantly affecting the heat-transport capacity of the alloy [12]. For Mg-Sn-Ca-based alloys, Sn and Ca exhibit distinct solute redistribution characteristics during solidification. Their segregation behavior directly affects the formation location, morphology, and continuity of second phases such as Mg_2Sn and CaMgSn. Further, it modifies the load-bearing capacity of grain boundaries and the solute state within the matrix [13]. During casting solidification, the grain-boundary wetting effect induced by solute segregation can markedly alter the alloy's hot tearing susceptibility. Meanwhile, the precipitation features of second phases at grain boundaries directly influence grain-boundary cohesion strength and high-temperature plastic deformability, which determine the cracking susceptibility of the alloy under solidification shrinkage stress. Existing studies have mainly focused on the effects of Sn content on the static mechanical properties and thermal conductivity of Mg-Sn-Ca alloys. Nevertheless, systematic investigations regarding the regulation of solidification behavior, hot-tearing susceptibility, and the synergy between strength-toughness and thermal conductivity by Sn remain relatively scarce.

In addition to alloy composition, the forming method is another critical factor affecting alloy performance. Conventional Permanent Mold Casting (PMC) generally produces dendritic α-Mg and interdendritic segregation microstructures. The continuous network of interdendritic second phases provides favorable paths for crack initiation and propagation [14]. In contrast, near-spherical primary α-Mg formed by semi-solid Rheo Die Casting (RDC) can weaken the microstructural inhomogeneity induced by the traditional dendritic skeleton and interdendritic segregation. It reduces casting defects, such as pores and hot tears, thereby mitigating local stress concentrations and crack propagation, thereby achieving desirable mechanical

properties [15, 16]. Cong et al. constructed a heterogeneous microstructure consisting of primary α-Mg, secondary α-Mg, and intergranular second phases via semi-solid rheo-diecasting, thereby improving the mechanical properties of magnesium alloys. Chang et al. [17] compared rheo-diecasting with conventional high-pressure diecasting and found that semi-solid rheo-diecasting can reduce casting defects such as oxide inclusions and significantly enhance ductility. In addition, the reduction in gas entrapment during semi-solid rheo-diecasting provides a microstructural foundation for further improving the mechanical and thermal conductivity properties of the material via subsequent heat treatment. Lang et al. [18] reported that the semi-solid die-cast Al-6Si-0.6Mg-0.1Sc alloy, after T6 heat treatment, exhibited marked improvements in microstructural morphology and internal lattice distortion, achieving simultaneous enhancements in mechanical performance and thermal conductivity. Although remarkable progress has been made in the design of compositions and process control of magnesium alloys in recent years, existing studies on magnesium alloys produced by RDC have primarily focused on comparing their microstructures and mechanical properties with those of HPDC-fabricated alloys. A systematic understanding of microstructural formation during RDC and its effects on the mechanical and thermal conductivity properties of magnesium alloys remains lacking. Meanwhile, the mechanism underlying the simultaneous improvement of mechanical and thermal conductivity properties via the RDC process requires further elucidation.

Therefore, in this study, Mg-xSn-0.2Ca-0.5Zr alloys (x = 3, 4, and 5 wt.%) were first fabricated via permanent mold casting. By comparing the grain size, phase composition, tensile mechanical properties, thermal conductivity, and hot-tearing susceptibility of the alloys, the optimal Sn content for the best overall performance was identified. Subsequently, the alloy with the optimal Sn content was selected to prepare semi-solid slurries using the Swirled Enthalpy Equilibration Device (SEED) method, followed by vacuum-assisted semi-solid rheo-diecasting and subsequent heat-treatment regulation. The evolution of the microstructure, as well as the laws governing changes in strength, ductility, and thermal conductivity, was systematically clarified, thereby achieving a synergistic improvement in mechanical properties and thermal conductivity.

This study aims to elucidate the underlying mechanism of the collaborative enhancement of mechanical and thermal conductivity in Mg-Sn-Ca-Zr alloys, thereby providing a theoretical foundation for the development of high-strength, high-thermal-conductivity magnesium alloys.

2. Experimental

2.1 Material fabrication

The experimental alloys were prepared using pure Mg (99.95 wt.%), pure Sn (99.7 wt.%), Mg–20Ca, and Mg–30Zr master alloys as raw materials (all compositions in this work are given in wt.% unless otherwise stated). Melting was conducted under a protective gas mixture of 0.5 vol.% SF_6 + 99.5 vol.% N_2. The nominal compositions were Mg-xSn-0.2Ca-0.5Zr (x = 3, 4, and 5 wt.%). Inductively coupled plasma optical emission spectrometry (ICP-OES) was employed to measure the actual composition of each alloy with three parallel replicates, and the results are listed in Table 1.

Table 1 Nominal and actual chemical compositions of the experimental alloys (wt.%).

Alloys	Sn	Ca	Zr	Mg
Mg-3Sn-0.2Ca-0.5Zr	2.82±0.17	0.18±0.05	0.41±0.09	Bal.
Mg-4Sn-0.2Ca-0.5Zr	3.89±0.12	0.17±0.03	0.39±0.14	Bal.
Mg-5Sn-0.2Ca-0.5Zr	4.85±0.15	0.18±0.04	0.36±0.19	Bal.

2.2 Permanent Mold Casting and Semi-solid Rheo Die-Casting

During PMC, pure Mg was melted at 720 ℃, followed by sequential additions of pure Sn, Mg–20Ca, and Mg–20Zr. After the raw materials had completely melted, the melt was cooled to 700 ℃ and held for 30 min. A metallic mold with a diameter and height of 75 mm was preheated to 200 ℃ and coated with BN. Casting was performed once the melt temperature had decreased to 680 ℃. PMC specimens were used to compare the solidified microstructure, tensile properties, and thermal conductivity of the 3Sn, 4Sn, and 5Sn alloys.

The melting procedure for RDC alloys was identical to that for PMC alloys. RDC

experiments were performed on an E53D Buhler horizontal cold-chamber die-casting machine equipped with a steel mold with a heating system. The mold and process parameters of this die-casting machine are shown in Figure 1. During the RDC trials, the mold temperature of the die-caster was set to 260 ℃, the melt pouring temperature was 700 ℃, and the injection speed was 3.8 m/s.

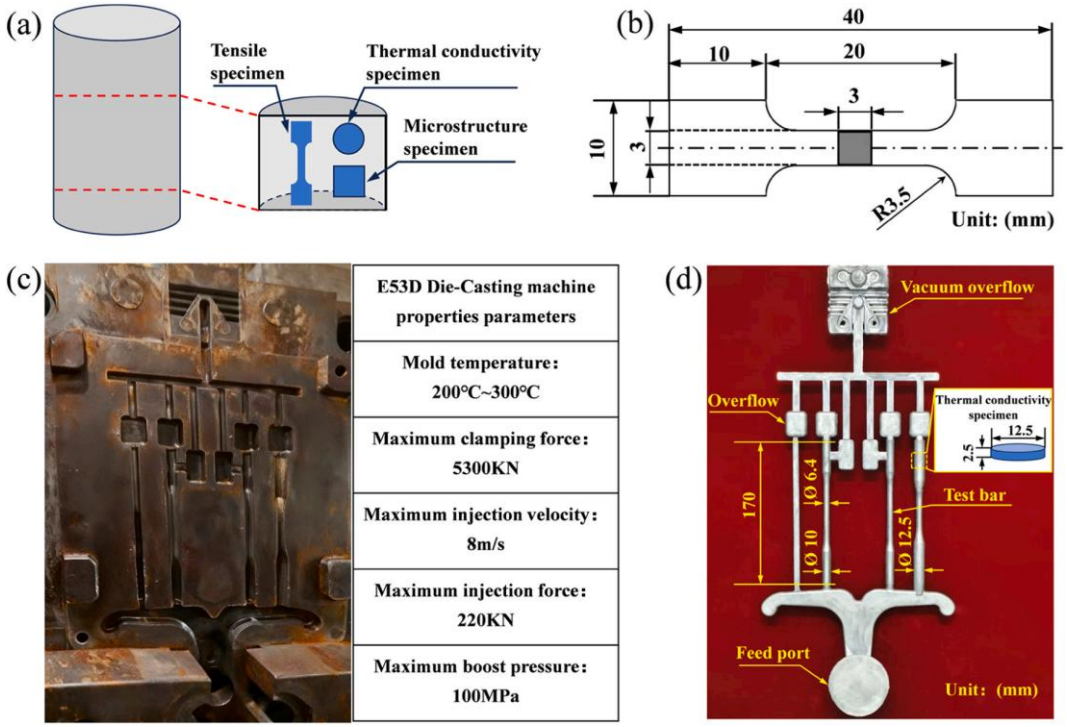

Figure 1 Specimens of PMC and RDC alloys: (a) PMC alloy ingot, (b) dog-bone-shaped tensile specimen, (c) die of die-casting machine and performance parameters, (d) RDC alloy specimen.

2.3 Hot-Tearing Susceptibility Test

As shown in Figure 2, a self-designed T-shaped hot-tearing mold based on the constrained rod method was adopted in this work, and a hot-tearing testing system was established with this mold as the core. The system consists of a load sensor, temperature sensors, a data acquisition system, and a computer. During solidification, the interaction between the solidification shrinkage force and mold constraints induces stress concentrations at the hot spot of the casting corner, which further initiate hot cracks that propagate inward from the outer surface. Meanwhile, the load and temperature sensors in the system can collect the shrinkage force and temperature signals in real time during alloy solidification. After the data acquisition module converts these signals into

identifiable digital information, the computer records and outputs the data as datasets and charts, which are used to analyze the initiation, propagation behavior, and mechanism of hot cracks. The detailed experimental procedures and mold configuration can be found in our previous studies [19, 20]. To ensure the accuracy and reliability of the experimental results, the hot-tearing tests on alloys with identical composition were repeated at least three times.

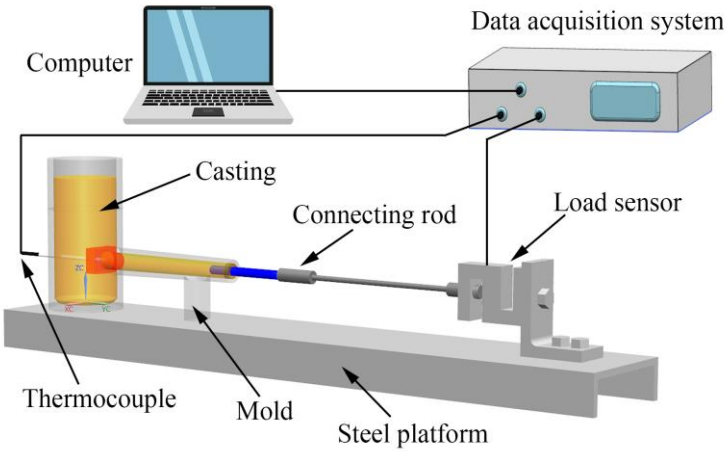

Figure 2 Schematic diagram of the hot tearing test system.

2.4 Heat Treatment

The T6 heat treatment of RDC specimens consists of solution treatment and artificial aging. First, the prepared specimens were placed in a YTH-12-12 box-type resistance furnace for solution treatment. After the castings were heated to the predetermined solution temperature and held for a designated duration, they were rapidly taken out and quenched in room-temperature water (approximately 23 ℃). Once the quenched castings were dried, they were transferred to an aging furnace for aging treatment. The castings were removed after reaching the preset aging temperature and holding for the scheduled time, completing the T6 heat treatment.

2.5 Microstructure and Phase Characterization

Metallographic specimens after grinding and mechanical polishing were etched using an ethanol solution containing 4 vol.% nitric acid. The microstructures of the alloys were then observed with a Zeiss Axio Observer A1 optical microscope (OM). A Hitachi S-3400N scanning electron microscope (SEM) equipped with an energy-

dispersive X-ray spectrometer (EDS) was used to characterize and analyze the microstructures and fracture morphologies. The phase constituents of the alloys were determined by an X-ray diffractometer (XRD) with Cu Kα radiation operated at 40 kV and 40 mA. The scanning range of the specimens was set from 20° to 90°, with a scanning rate of 2 °/min. Meanwhile, electron backscatter diffraction (EBSD; Zeiss Ge miniSEM 300, Jena, Germany) was adopted to characterize the microstructures of the samples. EBSD specimens were first mechanically polished, then electropolished in an electrolyte containing 10 vol.% perchloric acid and 90 vol.% ethanol at 15 V and −30 ℃.

2.6 Tensile Property and Thermal Conductivity Measurement

The room-temperature tensile specimens have a gauge length of 60 mm and a gauge diameter of 6.4 mm. Tensile tests were carried out on an EPT5101G universal testing machine at a crosshead speed of 1.5 mm/min in accordance with GB/T 228-2010. The elongation after fracture was calculated from the change in gauge length. The specimens for Brinell hardness measurement were machined to dimensions of 6.5 mm × 6.5 mm × 8 mm. A spherical indenter with a diameter of 2.5 mm was used under an applied load of 62.5 kgf and a dwell time of 10 s. The average value of five indentations was recorded for each specimen.

Specimens for thermal conductivity measurement were machined to dimensions of Φ12.5 mm × 2.53 mm. A Koreo CLA laser thermal conductivity analyzer was used to measure the room-temperature thermal diffusivity of the specimens. Graphite was sprayed on the specimen surface to enhance the absorption of laser pulse energy during measurement. Three test points were selected on each specimen, and the average value was adopted to represent the thermal diffusivity of the alloy. The density of alloy specimens was determined by the Archimedes method. The specific heat capacity was calculated according to the Neumann–Kopp law [21]. The thermal conductivity of the alloy, with units of W/(m·K), was calculated by Equation (1):

$$\lambda=\alpha\cdot\rho\cdot c_p \quad (1)$$

where α is the thermal diffusivity of the alloy in cm^2/s, ρ is the density of the alloy in g/cm^3, and c_p is the specific heat capacity of the alloy in J/(g·K).

3. Results

3.1 Microstructure of PMC Mg-xSn-0.2Ca-0.5Zr Alloys

Figure 3 shows the optical microstructures of permanent mold cast Mg-xSn-0.2Ca-0.5Zr alloys (x = 3, 4, 5 wt.%). It can be observed that alloys with different Sn additions exhibit typical dendritic solidification features and relatively coarse grains. Grain sizes were measured using ImageProPlus software. The average grain sizes of Mg-xSn-0.2Ca-0.5Zr alloys (x = 3, 4, 5 wt.%) are 202.27 μm, 142.31 μm, and 129.63 μm, respectively, indicating that the grain size gradually decreases with increasing Sn content. Meanwhile, distinct black elongated Sn-rich regions are distributed along the grain boundaries in the alloy microstructure. As the Sn content rises, the width and volume fraction of these Sn-rich regions increase progressively, and the amount of precipitated second phases in the alloys also increases.

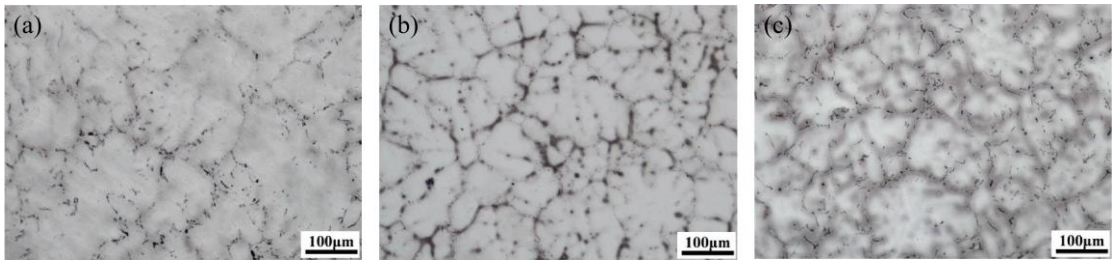

Figure 3 Optical micrographs of permanent mold cast Mg-xSn-0.2Ca-0.5Zr alloys with different Sn contents: (a) x = 3, (b) x = 4, and (c) x = 5 (wt.%).

Figure 4(a–c) shows the SEM images of permanent mold cast Mg-xSn-0.2Ca-0.5Zr alloys (x = 3, 4, 5 wt.%). The microstructures mainly consist of the α-Mg matrix phase and grayish-white secondary phases, with Sn-rich regions present at grain boundaries. The second phase is distributed both within the α-Mg matrix and along grain boundaries. Systematic statistics of the second-phase volume fraction were performed using Image ProPlus software. As the Sn content increases from 3 wt.% to 5 wt.%, the volume fraction of second phases in the alloys gradually rises to 1.24%, 2.23%, and 2.92%, respectively, indicating that increasing Sn content significantly promotes the formation of second phases.

Combining the EDS analysis (Fig. 4(d, e)) and XRD phase identification results (Fig. 4(f)), it can be concluded that all three alloys are mainly composed of α-Mg, Mg_2Sn, and CaMgSn phases. Among them, the acicular second phase corresponds to the CaMgSn phase, while the granular and rod-like second phases are Mg_2Sn. For the Mg-3Sn-0.2Ca-0.5Zr alloy, the solute concentration of Sn is relatively low. Ca preferentially reacts with the limited Sn to form CaMgSn; thus, the second phases are dominated by fine acicular CaMgSn, with only a small number of sparse, fine Mg_2Sn particles in a discrete distribution. When the Sn content increases to 4 wt.%, the enrichment of Sn solute raises the thermodynamic driving force for Mg_2Sn precipitation, increasing the distribution density of granular and short-rod Mg_2Sn, whereas CaMgSn still maintains an acicular morphology. The moderate cooling rate during permanent mold casting suppresses excessive coarsening and aggregation of second phases, resulting in their relatively uniform distribution along grain boundaries. In the Mg-5Sn-0.2Ca-0.5Zr alloy, however, the excess Sn solute transforms the growth mechanism of Mg_2Sn from nucleation-controlled to solute diffusion-controlled. Solute enrichment at grain boundaries accelerates the coarsening of Mg_2Sn, and some Mg_2Sn forms a semi-continuous network along grain boundaries. Meanwhile, CaMgSn also accumulates near grain boundary regions.

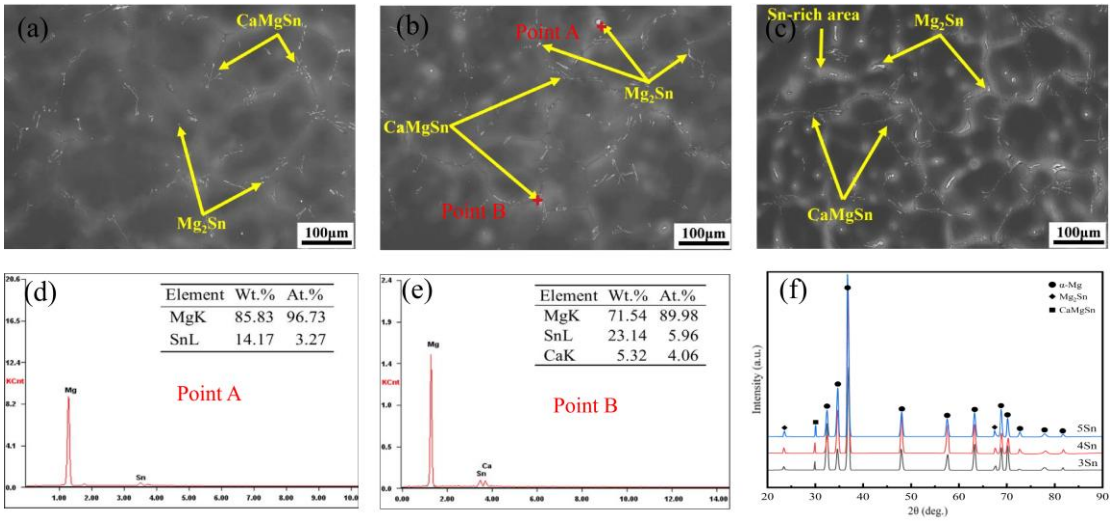

Figure 4 Permanent mold cast Mg-xSn-0.2Ca-0.5Zr alloys (x = 3, 4, 5 wt.%): (a–c) SEM images, (d, e) EDS analyses, and (f) XRD pattern.

3.2 Hot Tearing Susceptibility of the Alloys

Hot tearing is a typical and detrimental solidification defect that occurs during the late solidification stage of cast alloys and generally forms in the mushy zone where solid and liquid phases coexist. When the tensile strain induced by solidification shrinkage and thermal contraction exceeds the load-bearing capacity of the semi-solid skeleton, and the feeding of intergranular residual liquid is insufficient, cracks tend to initiate and propagate along grain boundaries covered by liquid films [22-24]. Therefore, the hot tearing behavior is essentially governed by the combined effects of solidification shrinkage, thermal strain, intergranular bonding state, and liquid feeding capacity. Studies have demonstrated that under identical solidification and constraint conditions, a higher critical shrinkage load for hot-tearing initiation usually indicates a stronger load-bearing capacity of the semi-solid skeleton. This facilitates improved resistance to hot tearing initiation and reduces the hot tearing susceptibility of the alloy [25].

Figure 5(a – c) presents the temperature-time-load curves and macroscopic hot crack morphologies at the hot spot of castings for Mg-xSn-0.2Ca-0.5Zr alloys (x = 3, 4, 5 wt.%). The hot tearing susceptibility tests were carried out at a mold temperature of 250 ℃ and a pouring temperature of 700 ℃. The peak solidification shrinkage load of the alloys first increases and then decreases with rising Sn content, among which the Mg-4Sn-0.2Ca-0.5Zr alloy achieves the highest peak load of 1320.65 N. Observation of macroscopic hot crack morphologies reveals that the 4Sn alloy exhibits the narrowest hot cracks. The hot crack volume measured by the paraffin infiltration method [26] (Fig. 5(d)) first decreases and then increases. The 4Sn alloy has the minimum hot crack volume of only 85 mm^3 . Comprehensive analysis demonstrates that the Mg-4Sn-0.2Ca-0.5Zr alloy exhibits the highest peak load and the smallest hot crack volume, indicating the lowest hot-tearing susceptibility. This alloy is more resistant to crack initiation and propagation during solidification, thereby exhibiting superior castability.

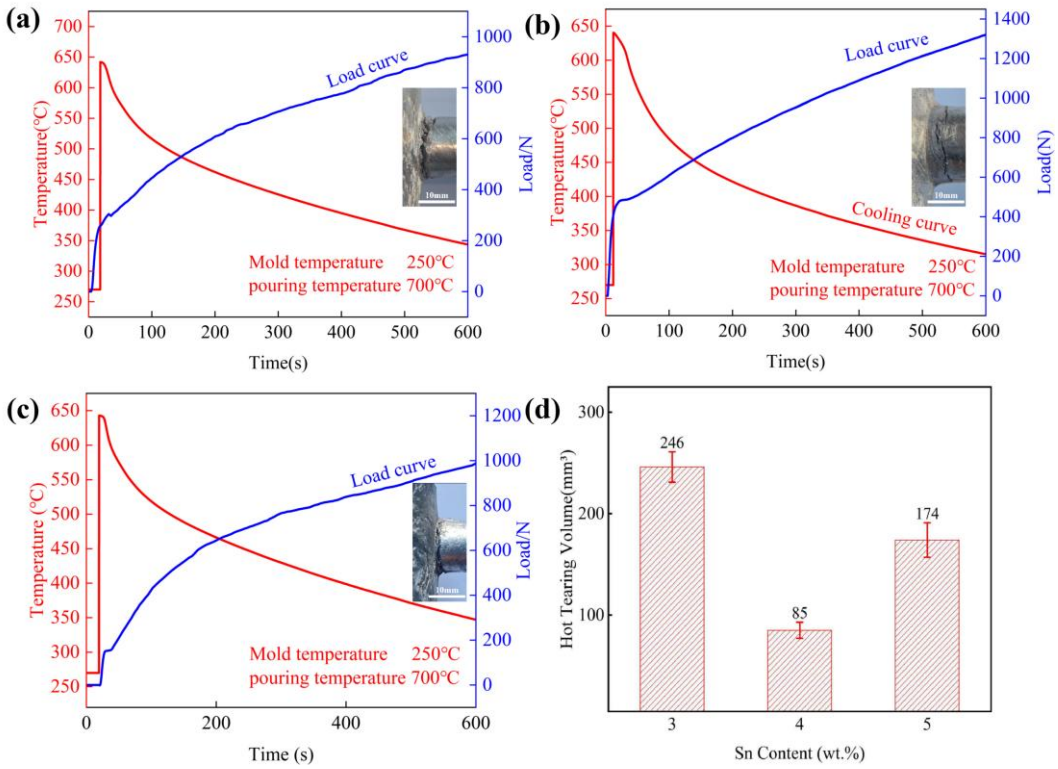

Figure 5 Hot tearing curves and macroscopic hot cracks (a–c), and hot crack volume (d) of Mg-xSn-0.2Ca-0.5Zr alloy castings (x = 3, 4, 5 wt.%).

3.3 Mechanical and Thermal Conductivity Properties

Figure 6(a) shows the stress–strain curves of permanent-mold-cast Mg-xSn-0.2Ca-0.5Zr alloys (x = 3, 4, 5 wt.%), and the corresponding data are summarized in Table 2. The ultimate tensile strength of the alloys first increases and then decreases as Sn content increases. The Mg-4Sn-0.2Ca-0.5Zr alloy exhibits the optimal comprehensive mechanical properties, with an ultimate tensile strength of 137 MPa, yield strength of 71 MPa, elongation of 7.6%, and thermal conductivity of 86.12 W/(m·K). Combined with the XRD phase analysis results, the precipitation amounts of the Mg_2Sn and CaMgSn second phases in the Mg-4Sn-0.2Ca-0.5Zr alloy increase significantly compared with the 3Sn alloy. The dispersion-strengthening effect of these second phases is fully activated, thereby improving the ultimate tensile strength of the alloys . When the Sn content increases to 5 wt.%, the grain size of the alloy is refined, while the amount of CaMgSn precipitation does not increase significantly. Nevertheless, the Mg_2Sn phase at grain boundaries undergoes substantial coarsening, forming a semi-continuous network structure. Previous studies [27, 28] have demonstrated that when

second phases are coarsened and distributed in a continuous or semi-continuous manner along grain boundaries, the deformation incompatibility between these phases and the α-Mg matrix readily induces dislocation pile-up and stress concentration near the phase interfaces. This promotes preferential initiation of microcracks at the matrix/second-phase interfaces; the microcracks then propagate along grain boundaries or second-phase-rich regions, eventually causing premature fracture and deteriorated plasticity of the alloy. Such a microstructure is detrimental to the overall mechanical performance. Figure 6(b–c) shows the variations in Brinell hardness and thermal conductivity of PMC Mg-xSn-0.2Ca-0.5Zr alloys (x = 3, 4, 5 wt.%). As the Sn content rises from 3 wt.% to 5 wt.%, the Brinell hardness increases gradually from 42.3 HBW to 50.8 HBW, whereas the thermal conductivity decreases steadily from 88.98 W/(m·K) to 79.71 W/(m·K). The rise in hardness originates from solid-solution strengthening of dissolved Sn atoms and stronger pinning of dislocation motion resulting from the increased volume fraction of second phases, including Mg_2Sn [12]. Conversely, the increased dissolved Sn concentration in the matrix and a greater number of phase interfaces induce more severe lattice distortion. The enhanced electron scattering by second phases consequently reduces the thermal conductivity [29]. Furthermore, although the hardness of the alloys increases continuously with increasing Sn content, both tensile strength and ductility decrease. This phenomenon may be associated with local stress concentrations and premature fracture induced by increased amounts and coarsening of second phases, such as Mg_2Sn [27]. Therefore, considering strength, ductility, hardness, and thermal conductivity comprehensively, the Mg-4Sn-0.2Ca-0.5Zr alloy exhibits superior overall performance and is selected as the base alloy for the subsequent semi-solid rheological die-casting investigation.

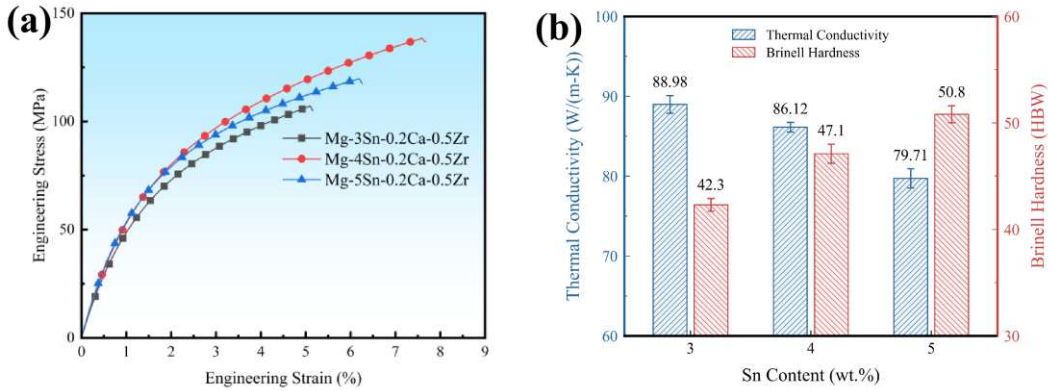

Figure 6 Stress–strain curves (a), hardness and thermal conductivity (b) of permanent-mold-cast Mg-xSn-0.2Ca-0.5Zr alloys (x = 3, 4, 5 wt.%).

Table 2 Mechanical properties of PMC Mg-xSn-0.2Ca-0.5Zr alloys (x = 3, 4 and 5 wt.%).

Alloys	UTS (MPa)	YS (MPa)	EL (%)	Hardness (HBW)
Mg-3Sn-0.2Ca-0.5Zr	107±4	60±4	5.1±0.2	42.3±0.6
Mg-4Sn-0.2Ca-0.5Zr	137±5	71±1	7.6±0.4	47.1±0.9
Mg-5Sn-0.2Ca-0.5Zr	119±2	75±2	6.2±0.5	50.8±0.8

3.4 RDC Mg-4Sn-0.2Ca-0.5Zr alloy and the influence of heat treatment

Figure 7 shows the SEM micrographs of semi-solid die-cast Mg-4Sn-0.2Ca-0.5Zr alloy. It can be observed that the matrix consists of near-spherical or ellipsoidal primary α-Mg grains with a uniform grain size distribution, and no obvious dendritic or irregular grains are found. The average grain size of the semi-solid die-cast Mg-4Sn-0.2Ca-0.5Zr alloy is measured to be 108.33 μm using Image Pro Plus software. Compared with the alloy prepared by permanent mold casting, the semi-solid die-cast alloy exhibits a smaller grain size and better uniformity in grain morphology. The second phases in the semi-solid die-cast Mg-4Sn-0.2Ca-0.5Zr alloy were analyzed by combining high-magnification SEM images, EDS spectroscopy, and X-ray diffraction (XRD) results (Fig. 8). As shown in Fig. 7(a), the second phase and Sn-rich regions of the semi-solid die-cast alloy are distributed along grain boundaries. According to the EDS results in Fig. 7(c, d), the blocky second phase at point A, located at grain boundaries, is identified as Mg_2Sn, and the elongated second phase at point B, along grain boundaries, corresponds to CaMgSn.

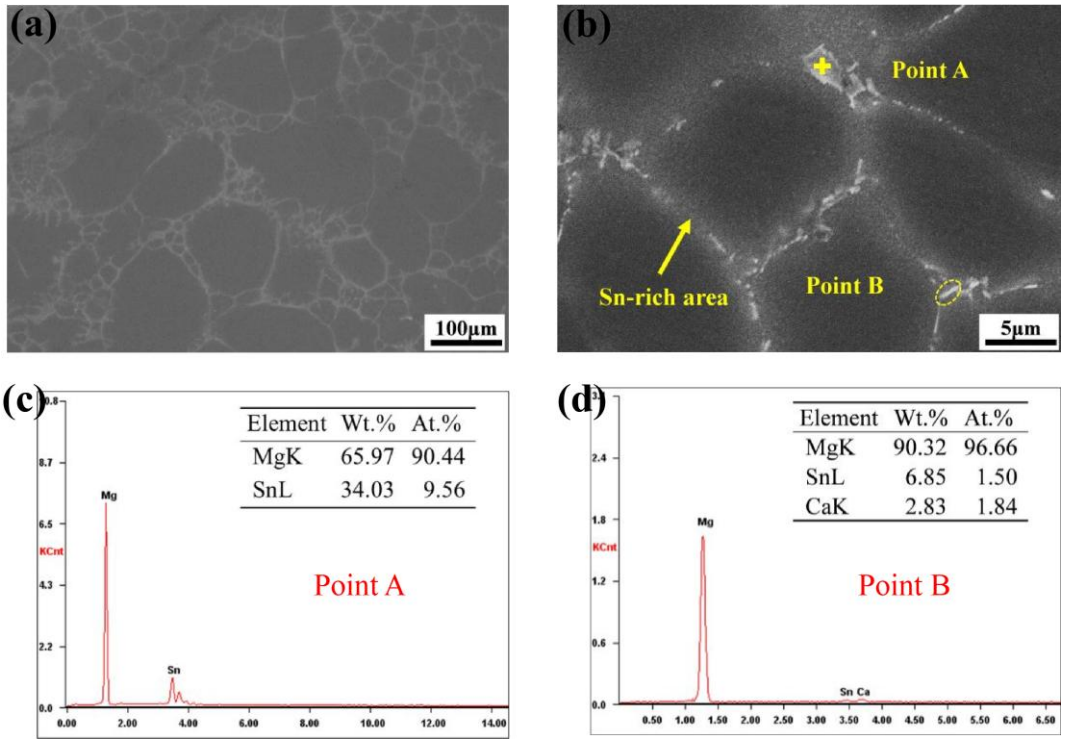

Figure 7 SEM micrographs and EDS analysis of semi-solid die-cast Mg-4Sn-0.2Ca-0.5Zr alloy.

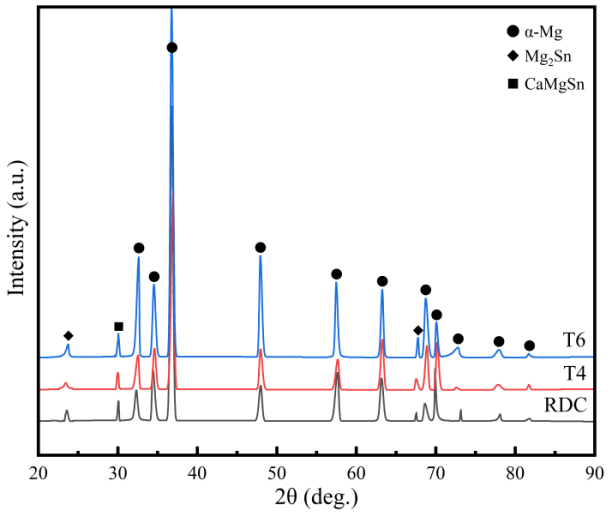

Figure 8 XRD patterns of semi-solid die-cast Mg-4Sn-0.2Ca-0.5Zr alloy under different heat treatment conditions.

Figure 9 shows the SEM micrographs of semi-solid die-cast Mg-4Sn-0.2Ca-0.5Zr alloy solution-treated at 400 ℃ with different holding durations. As observed in Fig. 9(a), the discontinuously distributed second phases at grain boundaries start to dissolve. The Mg_2Sn phase gradually dissolves into the α-Mg matrix, and the partial rod-like CaMgSn

phase also slightly dissolves into the matrix. As the solution holding time increases from 4 h to 8 h, Mg_2Sn continuously dissolves into the α-Mg matrix, whereas only limited dissolution occurs for the CaMgSn phase. This difference arises from the distinct thermodynamic stability and solution behavior between Mg_2Sn and CaMgSn phases. The solid solubility of Sn in α-Mg increases markedly with rising temperature; hence, solution treatment promotes the dissolution of Mg_2Sn and the reintroduction of Sn into the matrix [30, 31]. In contrast, CaMgSn possesses superior thermal stability. Meanwhile, Ca exhibits low solid solubility in α-Mg, so CaMgSn can remain stable after solution treatment [32]. At this solution temperature, slightly extending the holding time slightly increases the extent of CaMgSn dissolution, yet the phase cannot be fully dissolved into the α-Mg matrix, demonstrating its high thermal stability. Meanwhile, excessive extension of the solution-holding time facilitates grain growth and coarsening, weakening the grain-boundary strengthening effect and adversely affecting the strength and ductility of the alloys. When the solution holding time is prolonged to 12 h (Fig. 9(c)), more second phases dissolve into the matrix to form a supersaturated solid solution, while the degree of grain coarsening remains insignificant, achieving the optimal solution treatment effect. If the holding time further exceeds 12 h, although no obvious change occurs in the morphology of the second phases, the grain size shows a remarkable increase. Solution treatment for 12 h enables sufficient dissolution of second phases into the matrix and effectively avoids pronounced grain coarsening induced by prolonged holding. Therefore, 12 h is determined to be the optimal holding duration at this temperature. Subsequent aging treatment is carried out on this basis to improve the comprehensive properties of the alloy.

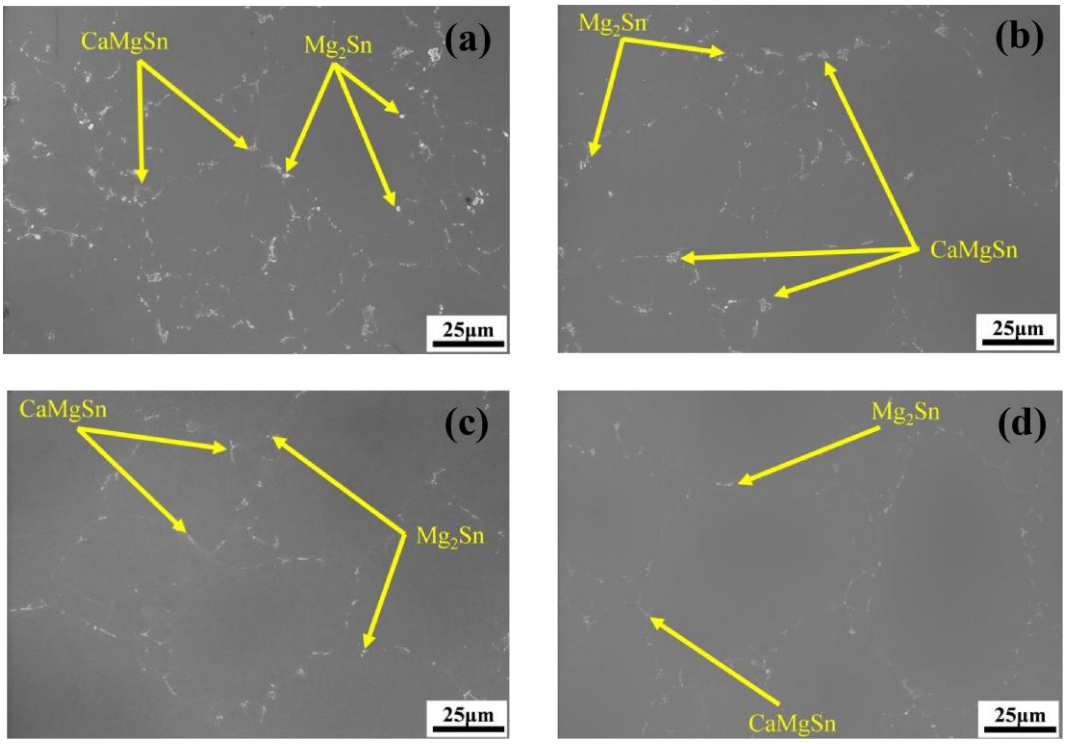

Figure 9 SEM micrographs of semi-solid die-cast Mg-4Sn-0.2Ca-0.5Zr alloy after solution treatment at 400 ℃ for different durations: (a–d) 4 h, 8 h, 12 h, and 16 h, respectively.

Figure 10 shows the SEM micrographs of semi-solid die-cast Mg-4Sn-0.2Ca-0.5Zr alloy subjected to solution treatment at 400 ℃ for 12 h, followed by aging at 175 ℃ with different holding durations. Based on the XRD patterns in Fig. 8 and the EDS results in Fig. 7, the second phases dissolved into the matrix during solution treatment precipitate at grain boundaries after the solution-aging treatment. The bright granular particles in the micrograph correspond to the Mg_2Sn phase, while the darker short-rod phases are identified as the CaMgSn phase. At the aging time of 6 h (Fig. 10(a)), the amount of precipitated second phases is low, and the aging strengthening effect is insignificant. After aging for 8 h (Fig. 10(b)), the solutes dissolved in the matrix during solution treatment continuously precipitate as granular second phases at grain boundaries. When the aging time reaches 10 h (Fig. 10(c)), the quantity of fine granular Mg_2Sn and short-rod CaMgSn phases at grain boundaries increases remarkably, and these phases are dispersively distributed along grain boundaries with relatively uniform distribution. When the aging time is prolonged to 12 h (Fig. 10(d)), pronounced coarsening and local aggregation of grain-boundary second phases occur, thereby

increasing microstructural inhomogeneity in grain-boundary regions. Previous studies [7] have demonstrated that overaging in Mg–Sn alloys promotes the coarsening of grain-boundary Mg_2Sn precipitates accompanied by the formation of precipitate-free zones (PFZs). Plastic strain tends to concentrate near grain boundaries, which triggers the premature initiation and propagation of intergranular microcracks. Moreover, interfacial debonding of grain-boundary precipitates further facilitates the formation of intergranular cracks, reduces the deformation compatibility and crack resistance of grain boundary regions, and ultimately degrades the mechanical properties of the alloy [33]. Overall, the optimal heat treatment regime is solution treatment at 400 ℃ for 12 h, followed by aging at 175 ℃ for 10 h. This regime promotes uniform, dispersed precipitation of second phases to fully exploit the precipitation-strengthening effect and inhibits the segregation of grain-boundary second phases, thereby providing a favorable microstructural basis for the simultaneous improvement in strength and ductility.

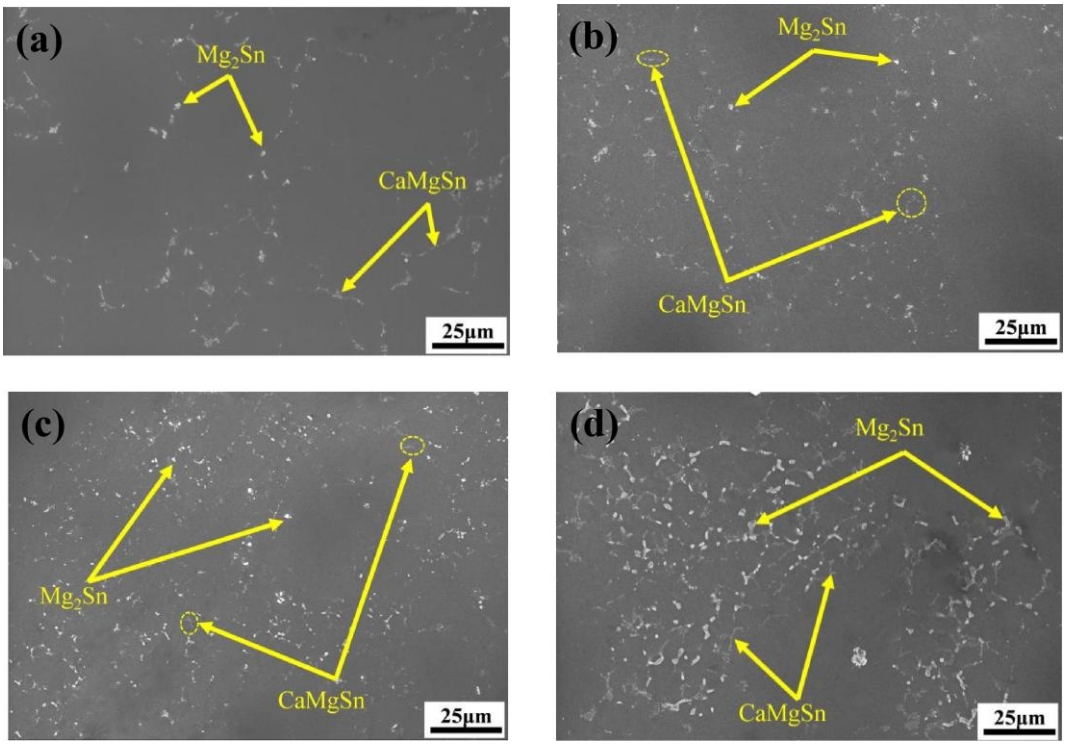

Figure 10 SEM micrographs of semi-solid die-cast Mg-4Sn-0.2Ca-0.5Zr alloy after solution treatment at 400 ℃ for 12 h and subsequent aging at 175 ℃ for different durations: (a–d) 6 h, 8 h, 10 h and 12 h, respectively.

3.5 Effect of heat treatment on the properties of RDG Mg-4Sn-0.2Ca-0.5Zr alloy

3.5.1 Mechanical properties

Figure 11(a,b) shows the stress–strain curves and Brinell hardness of semi-solid die-cast Mg-4Sn-0.2Ca-0.5Zr alloy after solution treatment at 400 ℃ for 12 h and subsequent aging at 175 ℃ for different durations. The corresponding data are summarized in Table 3. After T6 heat treatment (400 ℃ × 12 h solution + aging at 175 ℃), the mechanical properties of the semi-solid die-cast Mg-4Sn-0.2Ca-0.5Zr alloy first increase and then decrease with increasing aging time, and the optimal comprehensive mechanical properties are achieved at an aging time of 10 h.

At the aging time of 6 h, the ultimate tensile strength, yield strength, and Brinell hardness of the alloy are 171 MPa, 83 MPa, and 53.5 HBW, respectively, with an elongation of 13.2%. At this early aging stage, precipitates such as Mg_2Sn have not yet fully nucleated and grown, and their amount and dispersion are limited, so the precipitation strengthening effect cannot be fully exploited. Meanwhile, a high concentration of solute Sn remains in the matrix, and the alloy is mainly strengthened by the combined effect of residual solid-solution strengthening and incipient precipitation strengthening [7, 34]. As aging proceeds, the number of fine, dispersed Mg_2Sn precipitates gradually increases, thereby hindering dislocation motion and improving the alloy's strength and hardness [34]. The second phase moderately inhibits dislocation motion, and stress concentration is hardly induced, so the alloy maintains a high elongation.

When the aging time increases from 8 h to 10 h, the ultimate tensile strength and hardness continuously rise and reach peak values at 10 h (202 MPa, 60.2 HBW), the yield strength increases to 112 MPa, while the elongation only slightly decreases from 12.1% to 11.7%. At this stage, a large number of second phases precipitate in a dispersed manner, contributing to the continuous improvement of strength and hardness. Meanwhile, the uniformly dispersed second phases can effectively distribute stress and mitigate local stress concentrations, resulting in only a slight reduction in plasticity and achieving a favorable balance between strength and ductility. As the aging time is

extended to 12 h, the ultimate tensile strength drops to 189 MPa, the hardness decreases to 57.1 HBW, the yield strength decreases to 98 MPa, and the elongation decreases to 10.9%. This behavior originates from the segregation of second phases, which reduces their dispersion and weakens the pinning effect on dislocations, thereby decreasing the strength and hardness. Moreover, the segregated second phases readily serve as sites for crack initiation and propagation, further deteriorating ductility [35]. Therefore, aging time significantly affects the mechanical properties of the alloy by tuning the size, quantity, and spatial distribution of precipitates. In this work, the Mg-4Sn-0.2Ca-0.5Zr alloy aged for 10 h exhibits the optimal strength-ductility balance and comprehensive mechanical properties.

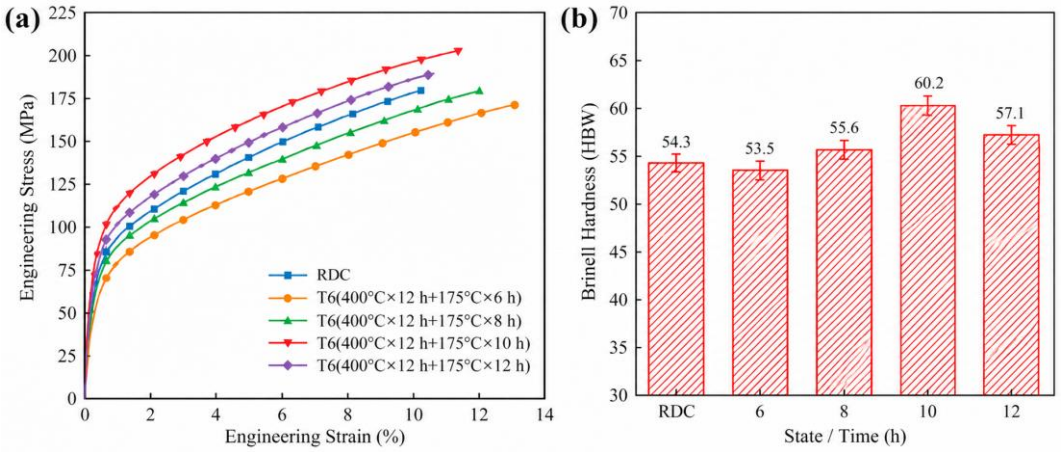

Figure 11 Stress–strain curves and hardness of semi-solid die-cast Mg-4Sn-0.2Ca-0.5Zr alloy after solution treatment at 400 ℃ for 12 h and aging at 175 ℃ for different durations: (a) stress–strain curves of the alloy, (b) hardness of the alloy.

Table 3 Mechanical properties of RDC Mg-4Sn-0.2Ca-0.5Zr alloy after solution treatment at 400 ℃ for 12 h and aging at 175 ℃ for different durations.

States	UTS (MPa)	YS (MPa)	EL (%)	Hardness (HBW)
RDC	181 ± 3	88 ± 2	10.2 ± 0.5	54.3 ± 0.6
400 ℃ × 12 h + 175 ℃ × 6 h	171 ± 4	83 ± 3	13.2 ± 0.4	53.5 ± 0.5
400 ℃ × 12 h + 175 ℃ × 8 h	180 ± 2	90 ± 2	12.1 ± 0.1	55.6 ± 0.9
400 ℃ × 12 h + 175 ℃ × 10 h	202 ± 3	112 ± 5	11.7 ± 0.2	60.2 ± 0.8
400 ℃ × 12 h + 175 ℃ × 12 h	189 ± 6	98 ± 4	10.9 ± 0.5	57.1 ± 0.6

3.5.2 Thermal conductivity

Figure 12 presents the measured room-temperature thermal conductivity of semi-solid die-cast Mg-4Sn-0.2Ca-0.5Zr alloy subjected to various heat treatments. The results reveal that the thermal conductivity decreases continuously as the solution holding time at 400 ℃ increases, reaching 93.43 W/(m·K) after 16 h of solution treatment. This trend primarily arises from the gradual dissolution of soluble second phases, such as Mg_2Sn, into the α-Mg matrix. The increased concentration of solute Sn induces severe local lattice distortion, which intensifies the scattering of charge carriers and lattice vibrations and shortens the mean free path. Previous studies on Mg–Sn and Mg-Sn-Ca alloys demonstrated that lattice distortion induced by solute atoms generally exerts a stronger effect on thermal conductivity than the second phases themselves [29]. Accordingly, the dissolution of second phases and the increased solute concentration in the matrix during solution treatment dominate the reduction in thermal conductivity.

Nevertheless, the thermal conductivity is markedly improved when the alloy pre-solution-treated at 400 ℃ for 12 h is subsequently aged. The maximum thermal conductivity of 112.35 W/(m·K) is obtained after aging for 12 h. This is because aging treatment promotes the extensive precipitation of Sn solute atoms, thereby alleviating lattice distortion in the α-Mg matrix. The reduction in lattice distortion facilitates the motion of electrons and phonons, the carriers of heat transfer, thereby significantly increasing the thermal conductivity of the alloys.

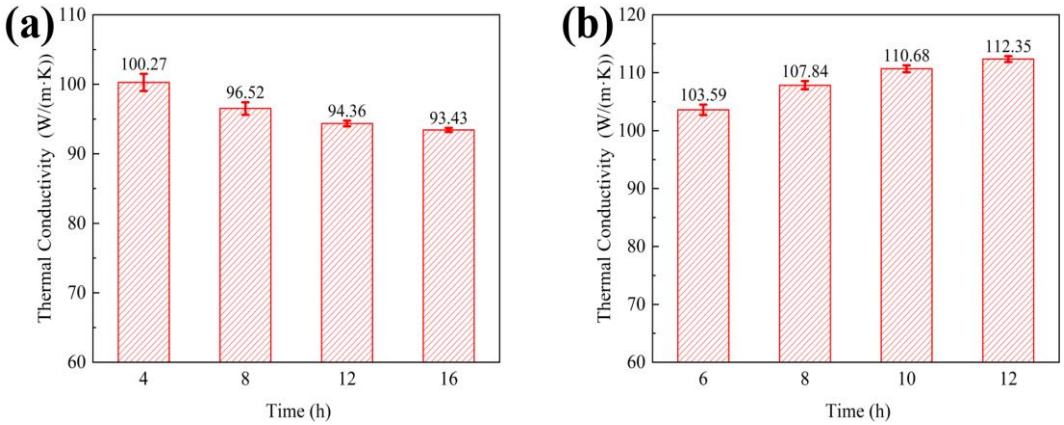

Figure 12 Thermal conductivity of semi-solid die-cast Mg-4Sn-0.2Ca-0.5Zr alloy under different heat treatments: (a) after solution treatment for different durations, (b) after aging treatment for different durations.

4. Discussion

4.1 Analysis of strength-toughness mechanism

4.1.1 Effect of grain size on mechanical properties of the alloy

Grain size is a key microstructural factor governing the strength and plastic deformation behavior of magnesium alloys [36]. Finer grains correspond to a greater number and denser distribution of grain boundaries. During plastic deformation of the alloy, grain boundaries pin dislocations and greatly increase resistance to dislocation motion, thereby improving the ultimate tensile and yield strengths via the grain-refinement strengthening mechanism [37].

Figure 13 shows the EBSD characterization results near the tensile fracture of semi-solid die-cast Mg-4Sn-0.2Ca-0.5Zr after T6 heat treatment (solution treatment at 400 ℃ for 12 h + ageing at 175 ℃ for 10 h). From the grain orientation map in Figure 13(a), the microstructure of the alloy consists of coarse primary α-Mg grains and finely dispersed secondary α-Mg grains. Combined with the KAM map in Figure 13(b) and the quantitative statistics in Figure 13(c), the overall average KAM value of the alloy is 1.07°. In this work, grains with a size below 35 μm are defined as secondary α-Mg grains (red grains in Figure 13(d)), while larger grains are primary α-Mg grains. Accordingly, the average KAM of primary α-Mg grains is 0.58° (Figure 13(e)), and the average KAM of secondary α-Mg grains is 1.23° (Figure 13(f)). It can be observed that high KAM values are mainly concentrated in the fine secondary α-Mg grain regions, which are markedly higher than those in the coarse primary grain matrix. This phenomenon is attributed to the smaller grain size and higher grain boundary density of secondary α-Mg grains, which can effectively accommodate and store abundant dislocation structures and thus greatly improve the work-hardening capacity of the alloy . During plastic deformation of the alloy, dislocation multiplication and interaction are enhanced within fine-grained regions, which significantly increases the resistance to dislocation slip and improves the alloy strength. Meanwhile, the inhomogeneous distribution of KAM values directly indicates obvious strain concentration around secondary α-Mg grains, further verifying that these regions strengthen the alloy via the work-hardening mechanism.

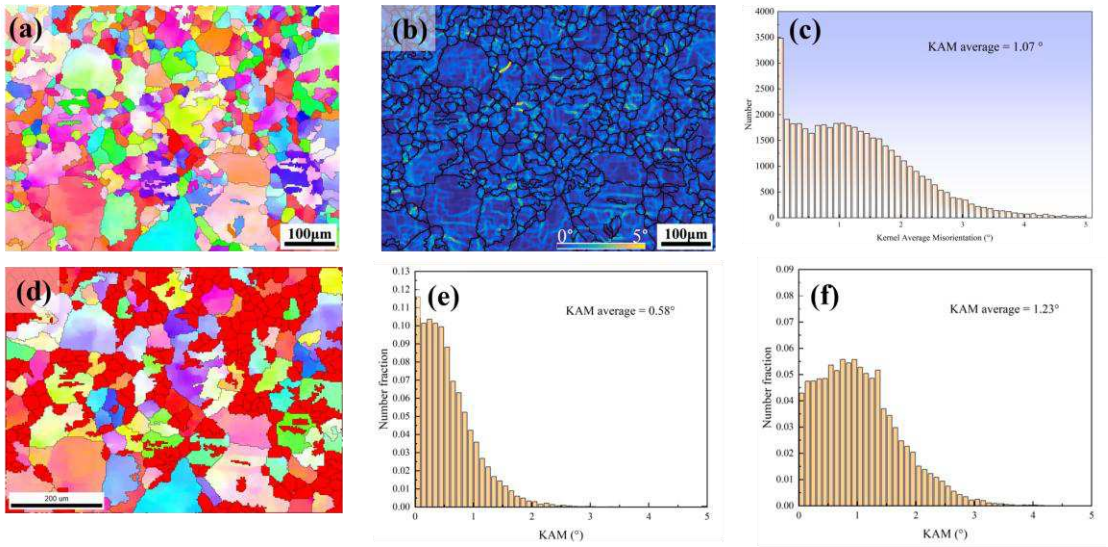

Figure 13 EBSD analysis results near the tensile fracture of semi-solid die-cast Mg-4Sn-0.2Ca-0.5Zr alloy after T6 heat treatment (400 ℃ × 12 h + 175 ℃ × 10 h): (a) inverse pole figure near tensile fracture, (b) KAM map, (c) KAM distribution of all grains, (d) map of primary and secondary grains, (e) KAM distribution of primary grains, and (f) KAM distribution of secondary grains.

4.1.2 Effect of second phases on mechanical properties of the alloy

After T6 heat treatmentment, the morphology of the second phases in the semi-solid die-cast Mg-4Sn-0.2Ca-0.5Zr alloy is modified, thereby further affecting the mechanical properties. In the untreated alloy, coarse blocky Mg_2Sn and elongated CaMgSn are mainly distributed continuously or semi-continuously along grain boundaries. The deformation incompatibility between hard, brittle second phases and the α-Mg matrix readily induces interfacial stress concentrations and crack initiation, thereby deteriorating the deformation compatibility of grain boundaries and reducing the plasticity and fracture resistance of the alloys [38, 39]. During solution treatment, coarse Mg_2Sn phases are largely dissolved into the α-Mg matrix, while CaMgSn remains mostly as refined residual particles owing to its high thermal stability. The subsequent aging treatment promotes the precipitation of supersaturated Sn to form fine granular or short rod-like Mg_2Sn with a dispersed distribution. The dispersed precipitates provide prominent precipitation strengthening by hindering dislocation motion. Meanwhile, the reduction in coarse, continuous second phases at grain boundaries alleviates interfacial stress concentrations and suppresses intergranular

crack initiation, achieving a good balance between enhanced strength and retained ductility [7, 10].

Figure 14 shows the tensile fracture morphologies of semi-solid die-cast Mg-4Sn-0.2Ca-0.5Zr alloy after solution treatment at 400 ℃ for 12 h and subsequent aging at 175 ℃ for different durations (6 h, 8 h, 10 h, and 12 h). Many tear ridges and small cleavage steps are observed on the fracture surface of the specimen aged for 6 h, indicating that the alloy maintains good ductility at this stage. After aging for 8 h, the number of cleavage steps increases while tear ridges decrease, reflecting the onset of ductility degradation. For the specimen aged for 10 h, clear cleavage planes appear on the fracture surface, the size of the cleavage steps further increases, and tear ridges are markedly reduced, suggesting a continuous deterioration in ductility. When the aging time is extended to 12 h, over-aging induces pronounced coarsening and grain-boundary segregation of second phases, thereby significantly reducing the intergranular bonding force. Cracks readily initiate at grain boundaries and propagate rapidly during tensile loading. Hardly any tear ridges can be observed on the fracture surface, and extensive cleavage planes are present, demonstrating that the alloy exhibits the lowest ductility at this condition.

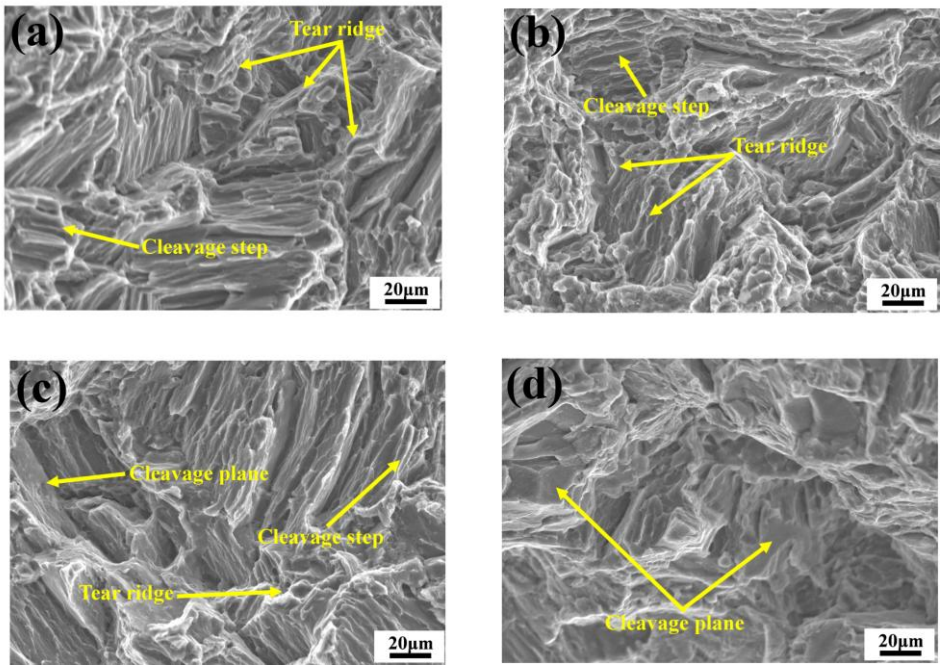

Figure 14 Fracture morphologies of semi-solid die-cast Mg-4Sn-0.2Ca-0.5Zr alloy after solution treatment at 400 ℃ for 12 h and ageing at 175 ℃ for different durations: (a–d) 6, 8, 10, and 12 h.

Figure 15 presents the room-temperature thermal conductivity, EDS composition of the α-Mg matrix, and the variation of lattice axial ratio (c/a) of semi-solid rheo-die-cast Mg-4Sn-0.2Ca-0.5Zr alloy under RDC, T4 (400 ℃ × 12 h), and T6 (400 ℃ × 12 h + 175 ℃ × 10 h) conditions. Table 4 summarizes the corresponding lattice parameters. The thermal conductivity of the alloy exhibits a clear trend of initially decreasing and then increasing with heat-treatment states, with a maximum of 110.68 W/(m·K) under the T6 condition. This variation shows a good correlation with the evolution of solute content and lattice parameters in the matrix. T4 treatment promotes the dissolution of soluble second phases, such as Mg_2Sn, into the α-Mg matrix, increasing the concentration of solute atoms dominated by Sn and enhancing local lattice distortion, thereby aggravating the scattering of charge carriers and reducing thermal conductivity [13]. The subsequent T6 aging facilitates the precipitation of supersaturated Sn from the matrix, forming Mg_2Sn, thereby reducing matrix solid solubility and weakening solute scattering. The α-Mg lattice gradually recovers, and its c/a ratio approaches that of pure Mg (c/a ≈ 1.6236), which markedly improves the heat transport capacity [29, 40].

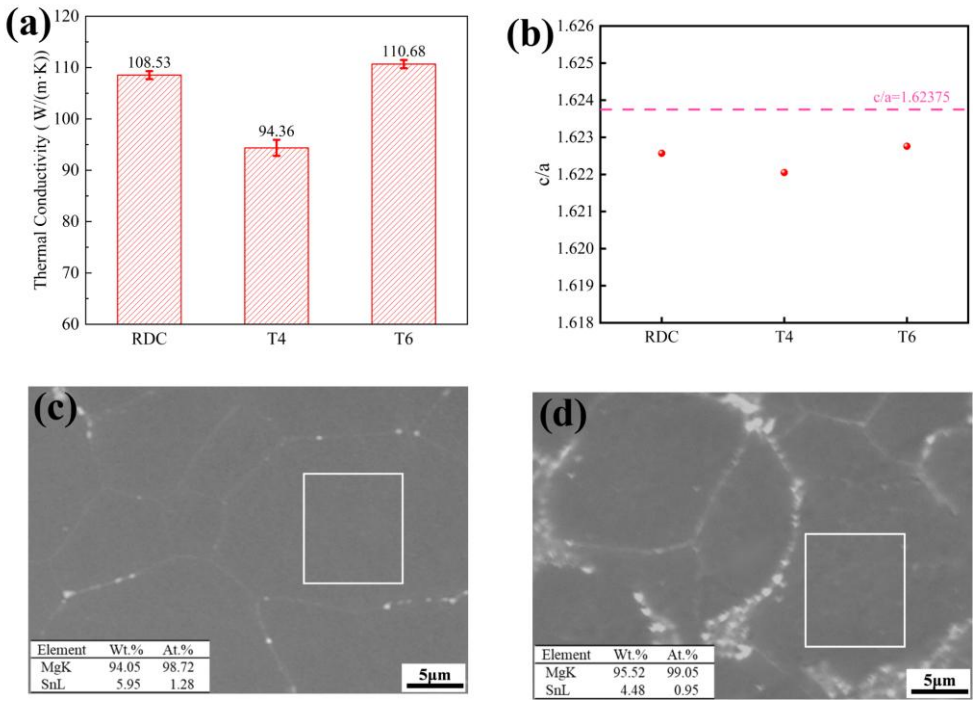

Figure 15 Thermal conductivity and matrix EDS analysis results of semi-solid die-cast Mg-4Sn-0.2Ca-0.5Zr alloy under different processes: (a) thermal conductivity of the alloy under different states, (b) lattice axial ratio (c/a), (c) T4 alloy (400 ℃ × 12 h), (d) T6 alloy (400 ℃ × 12 h) + 175 ℃ × 10 h)

Table 4 Lattice parameters and lattice axial ratio (c/a) of Mg matrix

Alloys	a(Å)	c(Å)	Lattice axis ratio
RDC	3.33413	5.40984	1.62257
T4	3.33624	5.41155	1.62205
T6	3.33972	5.41956	1.62276
Pure Mg	3.20936	5.2112	1.62375

Figure 16 compares the room-temperature tensile properties of cast Mg-Sn-based alloys. It can be seen that, compared with the rare-earth-containing cast/die-cast Mg-Sn alloys reported in the literature, the combination of semi-solid rheo-die casting and T6 heat treatment (400 ℃ × 12 h + 175 ℃ × 10 h) in this work further improves the comprehensive mechanical properties of the Mg-4Sn-0.2Ca-0.5Zr alloy. The alloy achieves an ultimate tensile strength of 202 ± 3 MPa and an elongation of 11.7 ± 0.2%, showing a good strength–ductility balance. Benefiting from the synergy of alloy composition optimization, regulation of the semi-solid solidification path, and subsequent heat treatment, the thermal conductivity reaches up to 110.68 W/(m·K). This study successfully develops a low-cost, rare-earth-free Mg–Sn-based alloy. The alloy achieves simultaneous improvements in strength and ductility while maintaining high thermal conductivity, thereby delivering outstanding comprehensive performance that integrates strength, ductility, and thermal conductivity.

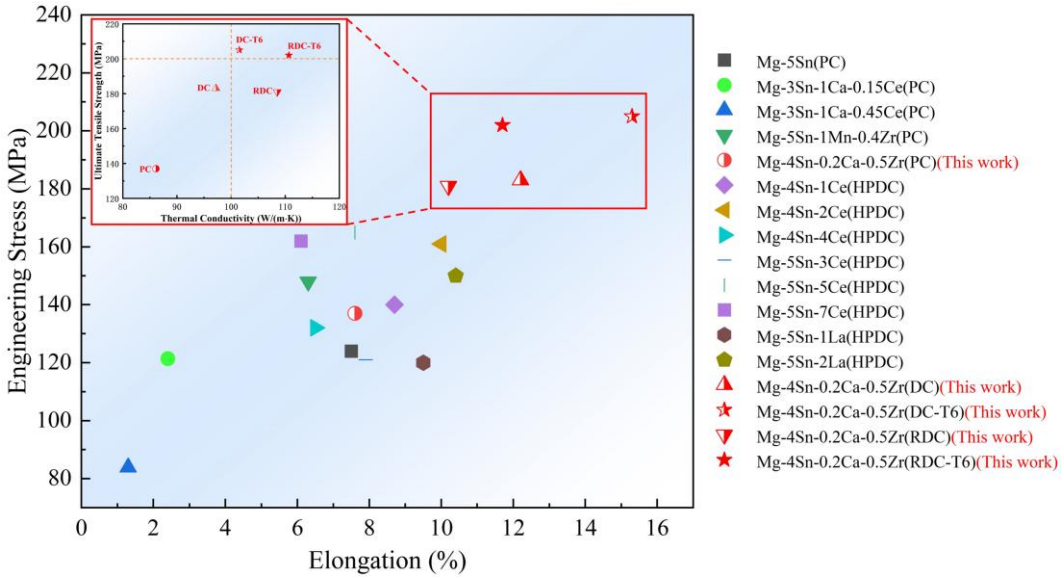

Figure 16 Comparison of room-temperature tensile properties of Mg-Sn based alloys.

5. Conclusions

Based on the microstructure and properties of permanent mold cast (PC) Mg-xSn-0.2Ca-0.5Zr alloys (x = 3, 4, 5 wt.%), semi-solid rheo-die casting (RDC) combined with heat treatment was adopted in this study to tailor the grain morphology and size, as well as the content, distribution, and morphology of second phases. Finally, a Mg-Sn-based alloy with high strength and high thermal conductivity was developed. The main conclusions are summarized as follows:

(1) For permanent mold cast Mg-xSn-0.2Ca-0.5Zr alloys (x = 3, 4, 5 wt.%), the grain size continuously refines with increasing Sn content. The alloy with 4 wt.% Sn exhibits the optimal comprehensive properties and the lowest hot-tearing susceptibility. Excessively high Sn content leads to coarsening of grain-boundary second phases with a semi-continuous network distribution, thereby inducing stress concentrations and deteriorating the alloy's ductility.

(2) Semi-solid rheo-die casting can produce round primary and secondary α-Mg grains. Fine secondary α-Mg grains possess higher grain boundary density, which can accommodate abundant dislocations and improve the work-hardening capacity of the alloy. The subsequent T6 heat treatment (solution at 400 ℃ for 12 h + aging at 175 ℃ for 10 h) enables refined and dispersed precipitation of Mg_2Sn phase, while CaMgSn phase maintains high thermal stability. After this treatment, the alloy achieves an ultimate tensile strength of 202 MPa, a yield strength of 112 MPa, and an elongation of 11.7%.

(3) T4 solution treatment promotes substantial dissolution of Sn into the α-Mg matrix, aggravating lattice distortion and enhancing electron scattering, which reduces thermal conductivity. The following T6 aging drives the precipitation of supersaturated Sn to form Mg_2Sn, reduces matrix solid solubility, restores the α-Mg lattice, and weakens carrier scattering. Consequently, the thermal conductivity of the alloy increases to 110.68 W/(m·K). As a result, the T6-treated Mg-4Sn-0.2Ca-0.5Zr alloy possesses both high thermal conductivity and favorable mechanical properties.

Acknowledgement

The authors would like to acknowledge the financial support from the Doctoral Research Initiation Fund Program of the Natural Science Foundation of Liaoning Province (2025-BS-0299), Basic Scientific Research Project of Liaoning Provincial Department of Education (Key Project) (LJ212610142016), Applied Basic Research Program of the Science and Technology Plan of Liaoning Province (2025080083-JH2/1013).

References

1. J. Yang, Z. Zhu, S. Han, Y. Gu, Z. Zhu, H. Zhang, Evolution, limitations, advantages, and future challenges of magnesium alloys as materials for aerospace applications. J. Alloys Compd. 1008, 176707 (2024). https://doi.org/10.1016/j.jallcom.2024.176707
2. A. Barakathulla, A. Elsayed, M. Easton, T. Abbott, J. Grandfield, H.Q. Ang, Conductivity of Cast Aluminium Alloys: A Review. Int. J. Metalcast. (2026). https://doi.org/10.1007/s40962-026-01931-5
3. W. Cong, F. Wang, X. Du, Z. Wang, L. Zhou, Z. Wei, P. Mao, J. Jiao, A novel approach to simultaneously enhancing the mechanical properties and thermal conductivity of magnesium alloys: Heterogeneous microstructures. J. Magnes. Alloys 16, 101995 (2026). https://doi.org/10.1016/j.jma.2026.101995
4. Q. Shang, J. Tan, H. Lv, Q. Dong, Y. Lin, G. Wu, A. Tang, B. Jiang, J. Eckert, Breaking the trade-off between thermal conductivity and strength of magnesium alloys: Mechanisms and strategies. Curr. Opin. Solid State Mater. Sci. 37, 101230 (2025). https://doi.org/10.1016/j.cossms.2025.101230
5. Y.L. Wang, Z.D. Zhang, Y.Y. Chang, M.X. Zhang, Y.D. Qu, S.L. Dong, The $\alpha_2 \rightarrow \gamma$ transformation in Ti-44Al-8Nb-0.1B alloy under lower temperature and lower triaxial compressive stress. Vacuum 251, 115359 (2026). https://doi.org/10.1016/j.vacuum.2026.115359
6. Y.Y. Chang, S.L. Dong, S.B. Liu, Y.D. Qu, R.R. Chen, G.L. Li, W. Zhang, S.R. Zhang, Different precipitation mechanism of B2 phase under three-way stress heat treatment. Mater. Charact. 236, 116395 (2026). https://doi.org/10.1016/j.matchar.2026.116395
7. Y. Deng, W. Sun, Y. Yang, H. Zhan, K. Yan, G. Zeng, Effects of Mg_2Sn precipitation on the age-hardening and deformation behaviour of a Mg-Sn-Al-Zn alloy. Mater. Sci. Eng. A 867, 144714 (2023). https://doi.org/10.1016/j.msea.2023.144714
8. Y.K. Kim, D.H. Kim, W.T. Kim, D.H. Kim, Precipitation of DO_{19} type metastable phase in Mg–Sn alloy. Mater. Lett. 113, 50–53 (2013). https://doi.org/10.1016/j.matlet.2013.09.005
9. J. Wang, J. Han, B. Du, Y. Huang, L. Sheng, W. Rao, C. Wang, X. Liu, Experimental and thermodynamic study of the Mg-Sn-Ca-Sr quaternary system: Part I-Mg-Sn-Ca ternary system. Calphad 58, 6–16 (2017). https://doi.org/10.1016/j.calphad.2017.03.008
10. X. Chen, D. Zhang, Y. Zhao, F. Pan, Q. Liu, Effect of microalloyed Ca on microstructure and

mechanical properties of Mg–6Zn–1Mn–4Sn (wt.%) alloy. J. Mater. Res. Technol. 17, 925–936 (2022). https://doi.org/10.1016/j.jmrt.2022.01.065

11. D.H. Kim, J.Y. Lee, H.K. Lim, J.S. Kyeong, W.T. Kim, D.H. Kim, The Effect of Microstructure Evolution on the Elevated Temperature Mechanical Properties in Mg-Sn-Ca System. Mater. Trans. 49, 2405–2413 (2008). https://doi.org/10.2320/matertrans.MER2008140
12. M.E. Moussa, R.N. Elshaer, The Impact of Sn Additions on Microstructure, Hardness and Wear Behavior of the As-Cast AZ41 Magnesium Alloy. Int. J. Metalcast. (2025). https://doi.org/10.1007/s40962-025-01819-w
13. C. Wang, Z. Liu, S. Xiao, Y. Chen, Effects of Sn, Ca additions on thermal conductivity of Mg matrix alloys. Mater. Sci. Technol. 32, 581–587 (2016). https://doi.org/10.1179/1743284715Y.0000000128
14. Z. Chang, Q. Deng, Q. Lan, J. Feng, D. Li, B. Liu, Y. Wu, L. Peng, W. Ding, Microstructure and mechanical properties of Mg-Gd-Y-Zn-Zr alloy prepared by rheo-diecasting. Mater. Sci. Eng. A 848, 143287 (2022). https://doi.org/10.1016/j.msea.2022.143287
15. Y. Gu, F. Wang, J. Jiao, Z. Wang, L. Zhou, P. Mao, Z. Liu, Study on Semisolid Rheo-Diecasting Process, Microstructure and Mechanical Properties of Mg-6Al-1Ca-0.5Sb Alloy with High Solid Fraction. Int. J. Metalcast. 18, 123–137 (2024). https://doi.org/10.1007/s40962-023-01001-0
16. J. Feng, B. Xing, Microstructural and Mechanical Characterization of AM60 Alloy in Semisolid Rheo-die casting with Varying Injection Velocity. Int. J. Metalcast. 18, 2533–2544 (2024). https://doi.org/10.1007/s40962-023-01197-1
17. Z. Chang, Q. Deng, Y. Wu, J. Feng, D. Li, X. Ren, H. Yu, X. Du, G. Wang, Y. Jin, Q. Lan, B. Liu, L. Peng, W. Ding, Semi-solid rheo-diecast Mg-xGd-3Y–1Zn-0.4Zr (wt%) alloys and their comparison with conventional HPDC alloys. J. Alloys Compd. 1003, 175508 (2024). https://doi.org/10.1016/j.jallcom.2024.175508
18. Z.H. Lang, F. Wang, X.D. Du, T.J. Song, Z. Wang, L. Zhou, P.L. Mao, Z.Q. Wei, J.W. Li, Effects of Sr/Ca Composite Modification and Heat Treatment Process on the Microstructure, Mechanical Properties and Thermal Conductivity of Semi-solid Al-6Si-0.6Mg-0.1Sc Alloy. Met. Mater. Int. 32, 681–697 (2026). https://doi.org/10.1007/s12540-025-01992-x
19. X.D. Du, Z.Y. Xu, F. Wang, S.W. Bai, L. Zhou, X.Q. Kang, Z. Wang, J.W. Li, Hot tearing behavior and mechanism of AXJ530 alloy under rotating magnetic field. J. Magnes. Alloys 13, 1757–1770 (2025). https://doi.org/10.1016/j.jma.2024.05.010
20. P.Y. Cheng, T.Y. Wu, X.D. Du, F. Wang, Z. Wang, L. Zhou, J. Jiao, Effect of Y Content on Hot Tearing Susceptibility and Mechanical Properties of Mg-6Al-1Ca-xY Alloys. Int. J. Metalcast. (2026). https://doi.org/10.1007/s40962-026-02101-3
21. J.M. Joubert, B. Kaplan, M. Selleby, The specific heat of Al-based compounds, evaluation of the Neumann–Kopp rule and proposal for a modified Neumann–Kopp rule. Calphad 81, 102562 (2023). https://doi.org/10.1016/j.calphad.2023.102562
22. W. Huang, B. Hu, Q. Zhang, H. Gao, J. Han, F. Yao, J. Wang, D. Li, X. Zeng, Research progress on hot tearing of magnesium alloys: Based on nucleation, propagation and feeding. J. Magnes. Alloys 16, 101969 (2026). https://doi.org/10.1016/j.jma.2025.101969
23. E. Liotti, A. Lui, T. Connolley, P.S. Grant, Probing interdendritic flow and hot tearing during solidification using real time X-ray imaging and droplet tracking. Acta Mater. 240, 118298 (2022). https://doi.org/10.1016/j.actamat.2022.118298

24. E. Giansante, A. Fabrizi, G. Timelli, Influence of Intermetallic Phases and Grain Refinement on Hot-Tearing Susceptibility in 6xxx-Series Aluminum Alloys. Int. J. Metalcast. (2026). https://doi.org/10.1007/s40962-026-02098-9
25. H. Zhong, Z. Lin, Q. Han, J. Song, M. Chen, X. Chen, L. Li, Q. Zhai, Hot tearing behavior of AZ91D magnesium alloy. J. Magnes. Alloys 12, 3431–3440 (2024). https://doi.org/10.1016/j.jma.2023.02.010
26. X. Guo, H. Zhao, J. Song, B. Jiang, W. Xie, J. Liao, H. Xie, J. Wang, J. Xiao, F. Pan, Effect of Ca on hot tearing susceptibility of WE43 alloy. J. Alloys Compd. 1002, 175451 (2024). https://doi.org/10.1016/j.jallcom.2024.175451
27. X. Zhuo, C. Shao, P. Zhang, Z. Hu, H. Liu, Effect of Hot Rolling on the Microstructure and Mechanical Performance of a Mg-5Sn Alloy. Materials 15, 5973 (2022). https://doi.org/10.3390/ma15175973
28. L. Feng, X. Dong, Q. Cai, S. Ji, Microstructure and Tensile Properties of HPDC Mg–RE Alloys with Varying Y Additions. Int. J. Metalcast. 18, 2893–2906 (2024). https://doi.org/10.1007/s40962-024-01266-z
29. H. Lv, J. Tan, Q. Yuan, F. Wang, Y. Zhou, Q. Dong, A. Tang, J. Eckert, B. Jiang, F. Pan, Recent advancements in thermal conductivity of magnesium alloys. J. Magnes. Alloys 12, 1687–1708 (2024). https://doi.org/10.1016/j.jma.2024.02.007
30. A. Dev, N. Naskar, N. Kumar, A. Jena, M. Paliwal, A systematic investigation of secondary phase dissolution in Mg–Sn alloys. J. Magnes. Alloys 7, 725–737 (2019). https://doi.org/10.1016/j.jma.2019.11.002
31. Y. Zhang, Y. Liu, S. Liu, H.-L. Chen, Q. Chen, S. Wen, Y. Du, Assessment of atomic mobilities and simulation of precipitation evolution in Mg-X (X=Al, Zn, Sn) alloys. J. Mater. Sci. Technol. 62, 70–82 (2021). https://doi.org/10.1016/j.jmst.2020.05.036
32. C. Wang, S. Guo, L. Zeng, D. Zheng, J. Xu, M. Yang, T. Liang, Effects of Second Phases on Microstructure, Microhardness, and Corrosion Behavior of Mg-3Sn-(1Ca) Alloys. Materials 12, 2515 (2019). https://doi.org/10.3390/ma12162515
33. W. Sun, Y. Deng, Y. Hu, H. Zhan, K. Yan, S. Shuai, E. Guo, Z. Zheng, G. Zeng, Enhanced high-temperature strength of a Mg-4Sn-3Al-1Zn alloy with good thermal stability via Mg_2Sn precipitation. J. Magnes. Alloys 15, 101643 (2026). https://doi.org/10.1016/j.jma.2024.12.024
34. Z. Shi, M. Zhang, X. Huang, X. Liu, W. Zhang, Research Progress in Age-Hardenable Mg-Sn Based Alloys. Acta Metall. Sin. 55, 1231–1242 (2019). https://doi.org/10.11900/0412.1961.2019.00049
35. X. Zhuo, L. Zhao, W. Gao, Y. Wu, H. Liu, P. Zhang, Z. Hu, J. Jiang, A. Ma, Recent progress of Mg–Sn based alloys: the relationship between aging response and mechanical performance. J. Mater. Res. Technol. 21, 186–211 (2022). https://doi.org/10.1016/j.jmrt.2022.08.126
36. H. Yu, Y. Xin, M. Wang, Q. Liu, Hall-Petch relationship in Mg alloys: A review. J. Mater. Sci. Technol. 34, 248–256 (2018). https://doi.org/10.1016/j.jmst.2017.07.022
37. H. Mirzadeh, Grain refinement of magnesium alloys by dynamic recrystallization (DRX): A review. J. Mater. Res. Technol. 25, 7050–7077 (2023). https://doi.org/10.1016/j.jmrt.2023.07.150
38. Z.-X. Zhao, Z.-M. Hua, D.-W. Li, D.-S. Wei, Y. Liu, J.-G. Wang, D. Luo, H.-Y. Wang, Effect of Sn Content on the Microstructure, Mechanical Properties and Corrosion Behavior of Biodegradable Mg–x (1, 3 and 5 wt.%) Sn–1Zn–0.5Ca Alloys. Materials 11, 2378 (2018).

https://doi.org/10.3390/ma11122378
39. R.Y. Na, Z.H. Tan, Y.M. Li, S.L. Dong, Y.D. Qu, Y.Z. Zhou, X.F. Sun, X.G. Wang, Microstructural evolution and failure mechanisms of low-cost third-generation single-crystal superalloy with PtAl coating. Surf. Coat. Technol. 529, 133457 (2026). https://doi.org/10.1016/j.surfcoat.2026.133457
40. C. Wang, Z. Cui, H. Liu, Y. Chen, W. Ding, S. Xiao, Electrical and thermal conductivity in Mg–5Sn Alloy at different aging status. Mater. Des. 84, 48–52 (2015). https://doi.org/10.1016/j.matdes.2015.06.110